Research Article Vol. 8, No. 5 / May 2021 / Optica 621

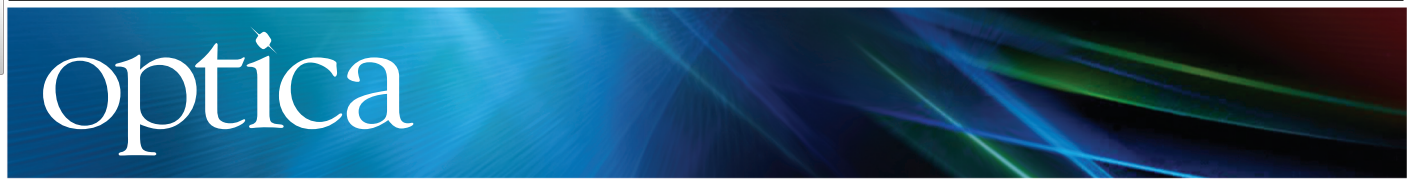

Gratingless integrated tunneling multiplexer for terahertz waves

Daniel Headland,[1] Withawat Withayachumnankul,[2] Masayuki Fujita,[1,*] and Tadao Nagatsuma[1]

[1]Graduate School of Engineering Science, Osaka University, Osaka 560-8531, Japan
[2]Terahertz Engineering Laboratory, School of Electrical and Electronic Engineering, The University of Adelaide, South Australia 5005, Australia
*Corresponding author: fujita@ee.es.osaka-u.ac.jp

Received 25 January 2021; revised 15 March 2021; accepted 15 March 2021 (Doc. ID 420715); published 29 April 2021

The arrayed waveguide grating (AWG) is a versatile and scalable passive photonic multiplexer that sees widespread usage. However, the necessity of a waveguide array engenders large device size, and gratings invariably commute finite power into undesired diffraction orders. Here, we demonstrate AWG-like functionality without a grating or waveguide array, yielding benefits to compactness, bandwidth, and efficiency. To this end, we exploit optical tunneling from a dielectric waveguide to an adjacent slab in order to realize a slab-confined frequency-scanning beam, which is manipulated using in-slab beamforming techniques that we have developed in order to separate distinct frequency bands. In this way, we devise an all-intrinsic-silicon integrated 4 × 1 frequency-division terahertz multiplexer, which is shown to support aggregate data rates up to 48 Gbit/s with an on–off-keying modulation scheme, operating in the vicinity of 350 GHz. Our investigation targets the terahertz range, to provide a critical missing building block for future high-volume wireless communications networks.

https://doi.org/10.1364/OPTICA.420715

1. INTRODUCTION

The terahertz range holds potential for ultra-wideband wireless communications applications, including 6G and beyond, due to large and under-utilized spectral bandwidth [1–4]. Terahertz communications will benefit from channelization [5,6], as individual channel bandwidths will be reduced, thereby simplifying baseband and intermediate-frequency (IF) circuits. Furthermore, passive multiplexers enable power combining of several independent sources at different frequencies, which is beneficial to terahertz technology because the achievable transmission distance is restricted by factors including limited power and strong path loss [7].

Direct frequency-division multiplexing of terahertz waves is challenging [6], and hence there are few reported demonstrations. One noteworthy example employed a leaky-wave antenna, and individual channels were collected with free-space optics, leading to a bulky system [8,9]. Terahertz diplexers based on hollow metallic waveguides have also been demonstrated [10,11], but the fabrication procedure is relatively complicated. Integrated solutions are preferable, and, to this end, recent progress in microstructured all-intrinsic-silicon terahertz waveguides is highly beneficial [12–18], as this material exhibits no Ohmic loss and near-negligible dielectric absorption ($\tan\delta \sim 0.00002$ at 1 THz). Furthermore, many passive terahertz components may be monolithically integrated within a given circuit and fabricated together in a single-mask etch process.

The development of all-dielectric platforms for terahertz waves opens the door to established passive nanophotonic multiplexers, such as arrayed waveguide gratings (AWG) [19,20]. Devices of this sort employ a dielectric slab as a free-propagation region to which several waveguides may connect. However, AWGs are electrically large, as they require two free-propagation regions that are connected in parallel by an array of curved waveguides. It is therefore impractical to physically scale such devices to the longer-wavelength terahertz range; a contemporary "ultra-compact" AWG [21] is $443 \times 675\lambda^2_{\text{central}}$, and hence it would occupy $\sim$2000 cm^2 if scaled to the 300 GHz band, and a typical four-channel AWG's footprint [22] would be $\sim$25,000 cm^2 ($2300 \times 1530\lambda^2_{\text{central}}$). Smaller devices are achieved with the sidewall-grating approach, where the waveguide array and one of the free-propagation regions are omitted, and the remaining slab region is fed in series via a grating at the sidewall of a channel waveguide [23–25]. Echelle gratings are another viable strategy to reduce device size [26,27]. However, such devices would still span several centimeters if scaled directly to the terahertz range. Furthermore, there are general issues associated with the use of grating techniques. Gratings exhibit multiple diffraction orders, and, hence, finite energy is invariably commuted into undesired directions. This also reduces bandwidth, as diffraction efficiency varies with frequency, and this effect is exacerbated by the sensitivity of fine grating structures to fabrication tolerances.

Here, we exploit leaky-wave principles for frequency differentiation. Terahertz waves optically tunnel from an unclad dielectric

waveguide to an adjacent silicon slab and form a frequency-scanning beam therein. The slab and waveguide are curved in order to focus this beam, thereby localizing specific frequency bands for isolation. Thus, we exploit the well-known phenomenon of optical tunneling in an entirely new way for gratingless in-slab beamforming, which commutes no power into undesired diffraction orders. This yields an efficient 300 GHz band 4×1 frequency-division multiplexer with a footprint area of 26×20 $\lambda^2_{\text{central}} \sim 4\,\text{cm}^2$—between three and four orders of magnitude smaller than a comparable AWG—and deploy it in a demonstration of terahertz communications. We also present a triplexer and a diplexer to illustrate the generality and scalability of the concept.

2. DESIGN CONCEPTS

A. Optical Tunneling

A micro-scale silicon waveguide is separated from an adjacent dielectric slab by a narrow air gap, as shown in Fig. 1(a). The thickness of the silicon is $t = 200\ \mu\text{m}$, the waveguide's width is $w = 160\ \mu\text{m}$, and the separation, s, is variable. The entire structure is surrounded by air, with no supporting substrate. The fundamental transverse-electric (TE) mode of the waveguide is employed, for which the electric field vector is parallel to the slab plane. In the absence of the slab, energy would be confined within this mode, and no power would be lost to the surrounding space. However, the slab couples with the evanescent fields of the waveguide's mode, and thereby captures a portion of confined power, which is commuted into the fundamental TE_0 mode. In this way, terahertz waves are progressively leaked from the waveguide to the slab, in a process known as optical tunneling [28]. Taken collectively, the waveguide and slab can be considered a form of leaky-mode structure [29].

Full-wave simulations using CST Studio Suite are employed to model the optical tunneling process, and resultant cross-sectional electric field distributions at frequencies of interest are shown in Figs. 1(b)–1(d). The fields that couple to the slab via optical tunneling are visible. Within the slab, field strength is observed to increase with respect to distance away from the waveguide, as power that is further away was leaked from the waveguide at an earlier position, and it will continue to grow indefinitely if infinite energy is supplied to a physically unbounded leaky-mode structure [29]. This phenomenon is particularly evident in Fig. 1(b), where the peak magnitude of fields in the displayed portion of the slab are observed to be stronger than those within the waveguide. This is because field confinement in the dielectric waveguide is reduced at lower frequencies, leading to an increase in interaction with the slab. Finally, minor variation is noted inside the slab structure, likely due to interference between the leaked beam and undesired fields from the mode launcher structure.

The complex propagation constant of the leaky mode is of key interest, as this describes its dispersion and rate of leakage, which are critical to in-slab beamforming. We also wish to determine how these properties are influenced by the separation, s. Propagation constants extracted from comparison of different lengths of waveguide are given in Figs. 1(e) and 1(f). It can be seen that both the phase constant and the rate of leakage increase with the proximity of the slab to the waveguide. Additionally, lower frequencies are observed to couple more rapidly because, for a dielectric waveguide in isolation, a greater proportion of modal fields occupy the surrounding space and, thus, field confinement is weaker. As such, the influence of the adjacent silicon slab is greater.

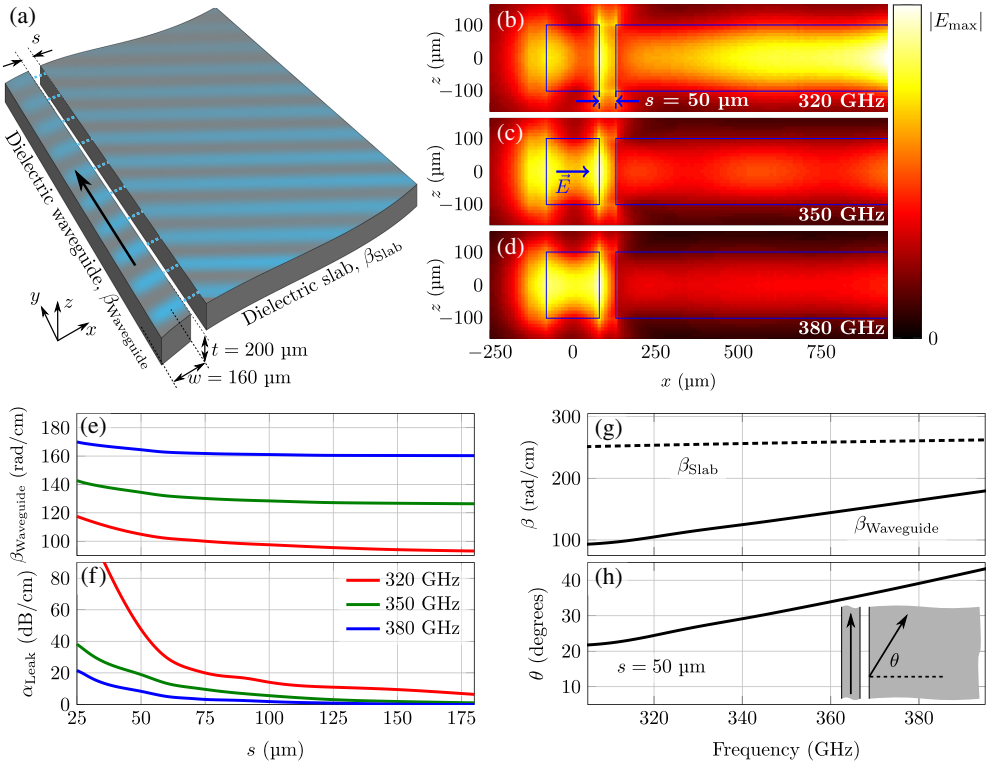

Fig. 1. Optical tunneling from unclad silicon dielectric waveguide to adjacent dielectric slab, showing (a) physical structure and illustration of optical tunneling process; (b)–(d) cross-sectional field distributions of the leaky mode, where $s = 50\ \mu\text{m}$; (e),(f) dispersion and leakage rate for a variety of separations, s; (g) dispersion with respect to frequency, where $s = 50\ \mu\text{m}$; and (h) scanning angle of the resultant slab-mode beam, where $s = 50\ \mu\text{m}$.

B. Leaky-Wave Principle

The radiation that enters the slab via optical tunneling will propagate away from the waveguide in the form of a slab-mode beam [30,31], which is analogous to a radiated beam in free-space, albeit confined into two dimensions in the xy plane of the silicon slab. As such, the optical tunneling process is closely related to a terahertz uniform leaky-wave antenna [32], as it launches a beam via progressive, continuous leakage from a guided wave into a free-propagation region. It is noted that conventional uniform leaky-wave antennas are necessarily implemented with fast-wave structures of less-than-unity modal index, in order to achieve spontaneous leakage [33]. On the other hand, the dielectric waveguide in the present work is slow wave. Slow waves do not leak spontaneously to free-space, and, hence, scatterers must be incorporated into the waveguide at regular intervals, thereby realizing a periodic leaky-wave antenna. In contrast to this, here we substitute the slab structure for free-space and achieve a slow-wave leaky-wave device that does not require scatterers.

The scanning angle of uniform leaky-wave structures is dependent upon the discrepancy in dispersion between the waveguide and the medium into which the beam is launched,

$$\sin\theta = \frac{\beta_{\text{Waveguide}}}{\beta_{\text{Slab}}}. \tag{1}$$

This angle, θ, is measured with respect to the normal of the interface between the two media. The phase constant of the leaky mode and the slab mode are given as a function of frequency in Fig. 1(g), for a nominal separation $s = 50$ μm. It can be seen that, as the leaky mode's dispersion is greater than the slab mode, its phase constant changes more rapidly with respect to frequency. According to Eq. (1), the angle at which the beam is launched also varies with respect to frequency, as shown in Fig. 1(h). This phenomenon facilitates the separation of distinct frequency components in the two-dimensional (2D) slab plane.

C. In-Slab Beamforming

The magnitude distribution of the slab-mode beam is engineered by tailoring the separation, s, along the length of the tunneling waveguide. In this work, the desired field distribution is a truncated Gaussian function, as it exhibits an acceptable compromise between high-aperture efficiency and low sidelobe level [34]. A $1/e$ Gaussian beam width of $w_{\text{Aperture}} = 6$ mm and a truncation magnitude of 50% are selected, resulting in the desired leaked-aperture magnitude distribution,

$$A(l) = \begin{cases} \exp\left[-\left(\frac{l-l_{\text{Max}}/2}{w_{\text{Aperture}}}\right)^2\right] & \text{if } 0 \le l \le l_{\text{Max}}, \\ 0 & \text{otherwise}, \end{cases} \tag{2}$$

along the uncurled waveguide length, l, as shown in Fig. 2(a). We employ an iterative procedure that is described in Section S2.1 of Supplement 1 to determine the appropriate profile of separation, s, along the waveguide length, and the result is given in Fig. 2(b). Separation is observed to progressively decrease, as power lost to leakage must be compensated by an increase in the rate of leakage. The procedure that is employed to tailor the separation also computes the expected resulting aperture magnitude distribution, and the results are shown in Fig. 2(a). It can be seen that the computed aperture distribution is in close agreement with the desired distribution up to the point at which the separation is reduced to $s = 10$ μm, which is the minimum viable separation according to fabrication constraints. At that point, it is no longer possible to increase the rate of leakage by reducing s so the leaked power is lower than desired thereafter. That said, this deviation is not expected to markedly degrade outgoing beam quality.

In previous work, focused beams have been launched from a leaky-wave antenna to free-space by tailoring the profile of the propagation constant [35] or by curving the geometry of the radiator [36]. Similarly, here we curve the boundary of the dielectric slab in order to achieve beam focusing within the slab itself. A target focus is selected, as shown in Fig. 2(c), and the distance from the slab boundary to this point is progressively shortened in order to compensate the phase that is acquired as the wave propagates within the dielectric waveguide. In this way, leaked power from all points along the curved slab boundary will constructively interfere at the target position, producing a focus at the design frequency, which is 350 GHz in this case. The details of this curving procedure are expounded in Section S2.2 of Supplement 1.

Owing to the leaky-wave phenomenon that is described in Section 2.B, the position of the focus is expected to progressively change as frequency deviates from 350 GHz. Put simply, different frequencies are projected towards different positions within the slab region. Full-wave simulations are performed in order to verify the existence of the frequency-scanning focus within the dielectric slab, and the results that are given in Fig. 2(d) indicate that the curved tunneling waveguide functions as intended. The field distribution along the inside of the slab boundary is also extracted from simulation and is plotted in Fig. 2(a) at the design frequency to facilitate comparison with expectations. It can be seen that reasonable agreement is attained. It is noted that the full-wave simulation results include effects such as reflection from the termination of the waveguide and interference from undesired fields that are coupled into the slab at the point where the waveguide mode is launched, which likely account for the minor discrepancies.

3. REALIZATIONS

A. Frequency-Division Multiplexer

In order to perform multiplexing, the frequency-scanning focus must be collected at specific distinct points that correspond to the foci of frequencies of interest and conveyed to separate dielectric waveguides, as shown in Fig. 3(a). Transitions are implemented by interrupting the slab region with linear-flared waveguide structures, to provide progressive index matching. Lower frequencies require larger flares. Following the transition, all waveguides are redirected using circular bends, such that they terminate in parallel, and with sufficient spacing to facilitate experimental probing. It is noted that the width of all waveguides is $w = 160$ μm to maintain consistency with the tunneling waveguide.

Following the examples of [14,17,18], subwavelength through-hole arrays are employed as a physical support structure. This essentially realizes a low-index effective medium, which can make contact with a given waveguide without disturbing the total-internal-reflection-based field confinement mechanism, thereby avoiding leakage or reflection. In this way, a buttress is implemented to support the input to the tunneling waveguide, as shown in Fig. 3(a). At the opposing end, little power remains in the tunneling waveguide, so it is terminated by attaching it directly to the slab region. The waveguides that support individual channels are collectively surrounded with a protective silicon frame, within

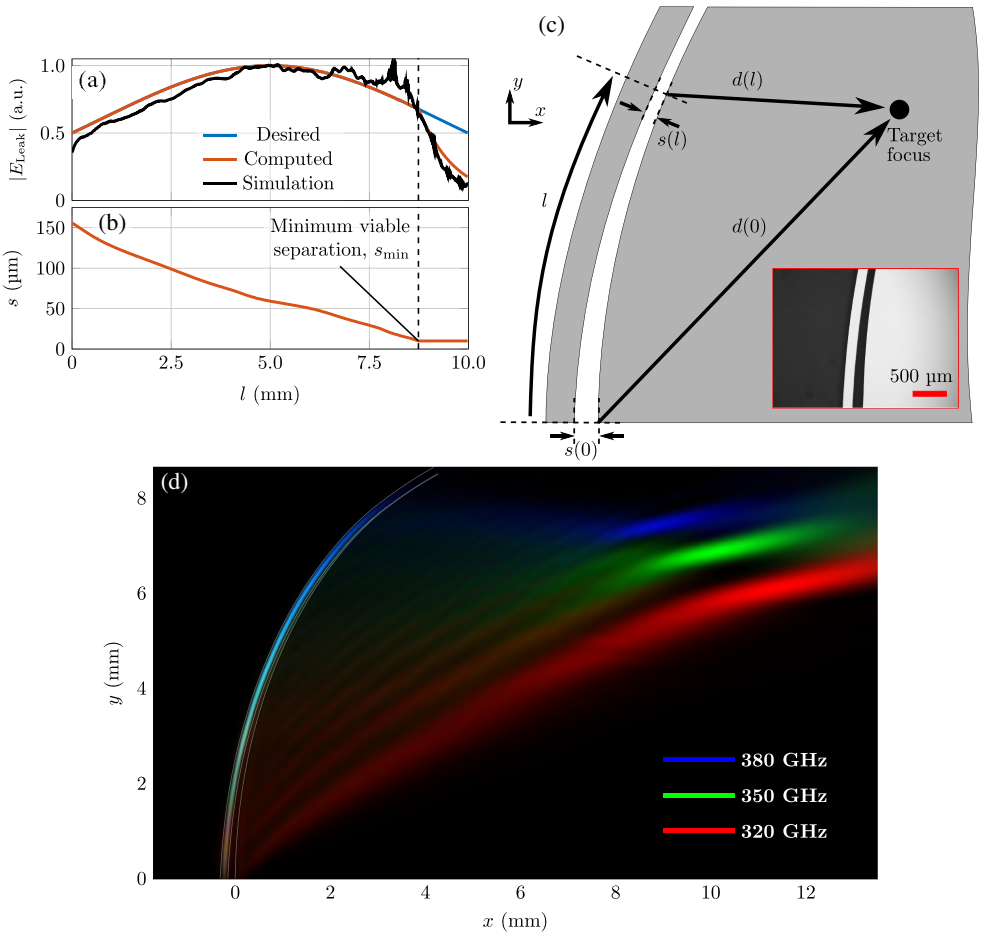

Fig. 2. Design of the in-slab focusing leaky-wave structure, showing (a) leaked-field magnitude distribution at the design frequency of 350 GHz and (b) the separation, s, as functions of uncurled waveguide length l; (c) an illustration of the design procedure for in-slab focusing, where the slab boundary is curved in order to compensate for accumulated phase in the silicon waveguide, as well as an inset micrograph of a fabricated structure; and (d) a false-color plot of the resultant field intensity distribution, i.e., Poynting vector magnitude, at $z = 0$, i.e., in the middle plane of the slab, where each component is in linear scale and normalized to its respective maximum.

which the low-index effective medium is implemented at the point of contact with the waveguides [17]. To facilitate experimental probing, all dielectric waveguides are terminated with 2-mm-long linear tapers with snub-width of 80 μm, for impedance matching purposes.

A four-channel terahertz tunneling multiplexer that is illustrated in Fig. 3(a) targets frequencies 318 GHz, 338 GHz, 358 GHz, and 378 GHz. The commercially available CST Studio Suite software package is employed for full-wave simulations that investigate the device's functionality, and resultant field intensity distributions are given in Figs. 3(b)–3(e). It can be seen that power is routed to distinct channel ports, as intended. Simulated magnitude transmission is given in Fig. 3(f), showing efficiencies of ∼66%, ∼71%, ∼78%, and ∼81%, as well as 3 dB channel bandwidths of ∼18 GHz, ∼14 GHz, ∼13 GHz, and ∼20 GHz, for channels 1–4, respectively. Efficiency is defined as the proportion of stimulated power that successfully undergoes transit through the multiplexer itself at the center frequency of the relevant channel. This is currently limited by reflection from the waveguide flares and will likely increase with further refinements to the design.

The thermal stability of the multiplexer device is of interest, and, in particular, the degree to which thermal effects may impact the frequency selectivity of each channel. Thermal expansion of single-crystal silicon [37] is investigated in simulation, and details are given in Section S3 of Supplement 1. It is found that an increase of 200°C over room temperature produces a downward frequency shift of less than 0.35 GHz for all channels of the multiplexer. We consider this shift to be of low significance, as it is ∼0.1% of the center frequency of the multiplexer device. Thus, the multiplexer exhibits high thermal stability. The reason that the frequency shift is downward, rather than upward, is because thermal expansion increases the cross-sectional area of the tunneling waveguide, thereby reducing its dispersion. We also wish to remark that variation in the terahertz-range refractive index of silicon due to thermal effects is minimal [38], and it is therefore not expected to exert a significant impact upon thermal stability.

The multiplexer design is fabricated using deep reactive ion etching [13]. Substrateless, unclad silicon microbeams serve as channel waveguides and are sufficiently robust to be self-supporting provided there is anchorage to the integrated protective frame [17]. The fabricated devices are manually handled using ordinary tweezers that make contact with the un-etched portions of the protective frame, exclusively. It is noted that, when deployed in practical applications, these tweezers will be replaced with a packaging structure that clamps to the frame [18].

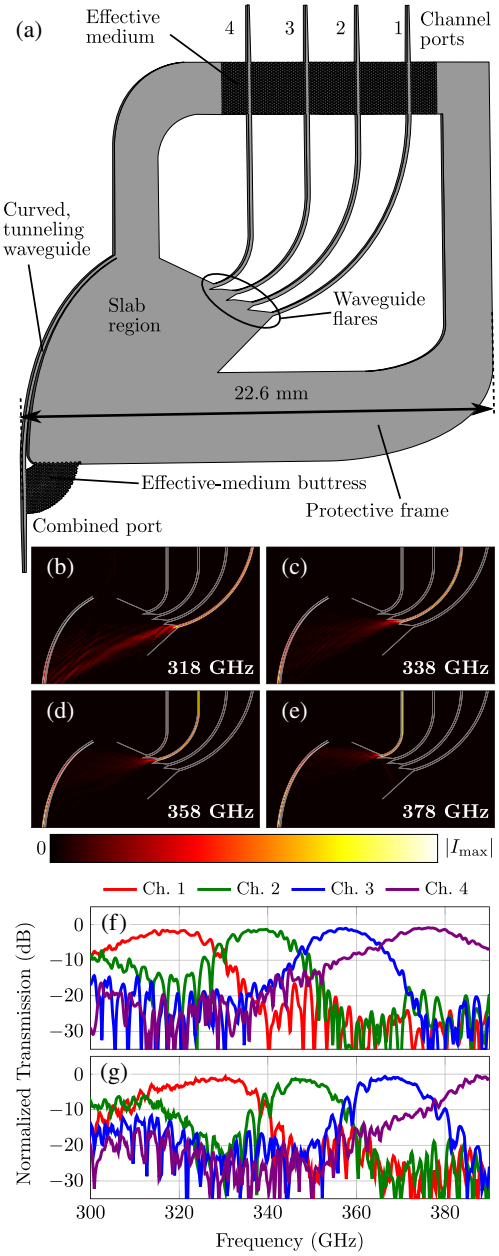

Fig. 3. Terahertz tunneling multiplexer device with uncurled tunneling waveguide length $l_{Max} \sim 10$ mm (i.e., leaked-aperture Gaussian beam width $w_{Aperture} = 6$ mm): (a) schematic illustration, (b)–(e) simulated field intensity, i.e., Poynting vector magnitude, $|I|$, in the linear scale and normalized to their respective maxima, and (f),(g) simulated and measured transmission.

During experimental characterization, the taper at the combined port is coupled to a terahertz source via a hollow metallic waveguide of inner conductor dimensions of 711 μm × 356 μm, corresponding to operation in the range from 260 GHz to 400 GHz. Alignment is performed manually using micrometer stages. The taper structures provide broadband index matching to the fast-wave fundamental mode of the hollow waveguide, thereby suppressing reflections at this interface. The source generates terahertz power by 9× frequency multiplication of a millimeter (mm)-wave signal, which is swept from 33.3 GHz to 43.3 GHz, thereby producing frequencies from 300 GHz to 390 GHz. Following transit through the multiplexer device, the terahertz waves are collected by a second hollow metallic waveguide that is coupled to one of the channel ports. The terahertz signal is then down-converted via mixing with a 36×-multiplied microwave-range local oscillator and subsequently inspected using a spectrum analyzer. For normalization purposes, a fabricated silicon reference device consists of a short length of silicon waveguide that is terminated with a supporting buttress at one end and effective-medium cladding at the other. The transmission through this device is measured, and the result is employed to remove the influence of coupling loss. As such, the measured results essentially isolate the response of the multiplexer itself. This is appropriate as the multiplexer is the primary subject of this work, whereas the coupling structure itself is of little scientific interest. Furthermore, this particular coupling mechanism is chosen solely as a means to probe the multiplexer's response in broadband, whereas in the case of practical deployment, it will be incorporated within a larger integrated terahertz system that contains many components that are interconnected with silicon waveguides. It is also noted that a similar process of normalization is performed with the simulated results given in Fig. 3(f), using a simulated model of the fabricated reference structure for which the simulated transmission magnitude is given in Section S4 of Supplement 1.

Measured transmission is shown in Fig. 3(g), and it can be seen that channelization is successfully achieved and that efficiency and bandwidth are comparable to simulation. However, there is a discrepancy; in measurement, each channel has been shifted upwards in frequency by ∼10 GHz. We ascribe this to over-etching, which narrows the tunneling waveguide and thereby increases the disparity in dispersion between the silicon waveguide and the slab. Evidence for this over-etching is provided in Section S5 of Supplement 1.

The isolation performance is defined as the minimum contrast in transmission magnitude between the peak of a given channel and that of the other channels at the same frequency. Hence, the isolation is at least 14 dB at the center frequency of each channel. Factors that limit the isolation of the tunneling multiplexer involve spillover between the closely spaced adjacent waveguide flares and evanescent interaction between adjacent waveguides as they undergo circular bending. In the future, such effects may be mitigated by refinements to the geometry of the single-channel waveguides and their interface to the slab region and by the integration of photonic filters. Evanescent interaction may also be reduced by including a broadband photonic bandgap structure [15] between adjacent waveguides or by simply widening the track in order to increase confinement. Finally, the leaked-aperture distribution may be optimized in order to produce a focused beam that minimizes spillover between adjacent channels.

B. Channel Scalability

It is well known that the width of a focused beam is dependent upon the ratio of aperture size to focal length [39]; a fixed ratio will produce a specific beam size—irrespective of absolute focal length. By the same rationale, if we reduce the uncurled length of the tunneling waveguide, l_{Max}, whilst proportionally decreasing the distance from the target focus to the origin, $d(0)$, then the size of the in-slab beam's focus will not change. On the other hand, the length of the path that is described by the focused beam will be reduced in approximate proportion with l_{Max}. These two effects result in greater overlap between adjacent frequencies, as the focused beam scans more gradually with respect to frequency. As

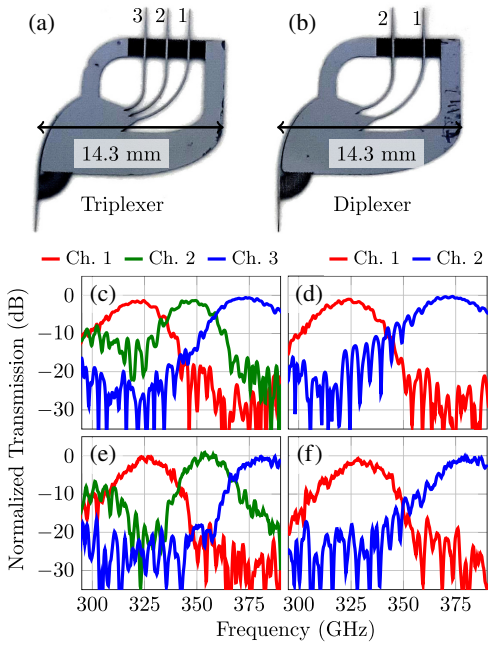

Fig. 4. Demonstration of the scalability of the tunneling multiplexer concept, showing (a),(b) photographs of tunneling multiplexers, for which the Gaussian beamwidth of the leaked-aperture distribution is reduced to $w_{\text{Aperture}} = 4$ mm, corresponding to uncurled tunneling waveguide length $l_{\text{Max}} \sim 6.7$ mm; (c),(d) simulated and (e),(f) measured transmission of the triplexer and diplexer.

a consequence, the bandwidth of individual channels is increased, and the number of channels that may be included is decreased. Conversely, if a larger number of lower-bandwidth channels is desired, then this may be achieved by increasing the length of the tunneling waveguide.

In order to demonstrate the scalability of the concept, tunneling multiplexers are devised by repeating the design procedure with the Gaussian beamwidth of the leaked-aperture distribution set to $w_{\text{Aperture}} = 4$ mm, rather than the 6 mm employed for the device shown in Fig. 3. Both a triplexer and a diplexer are devised in this way, and photographs of the fabricated devices are shown in Figs. 4(a) and 4(b), respectively. The sole difference between these two devices is their arrangement and number of channel ports; the tunneling waveguide portions are identical. Simulated transmission is shown in Figs. 4(c) and 4(d) and measured results in Figs. 4(e) and 4(f). The operation of these smaller multiplexers is confirmed from these results, and it can be seen that the channel bandwidth is indeed enhanced, as intended. As in the case of the four-channel multiplexer presented in Fig. 3, all measured channels have been shifted upwards in frequency with respect to simulation due to over-etching.

C. Communications

A demonstration of terahertz-range communications is performed in order to determine whether digital information at high data rates may be supported by the multiplexer, as is its intended application. A two-color infrared laser signal is optically modulated with non-return-to-zero on–off keying, using a pseudo-random bit sequence that originates from a digital pulse-pattern generator, and is 2^9-1 bits long. This light signal is applied to a uni-traveling-carrier photodiode (UTC-PD), which is a photomixing terahertz source that

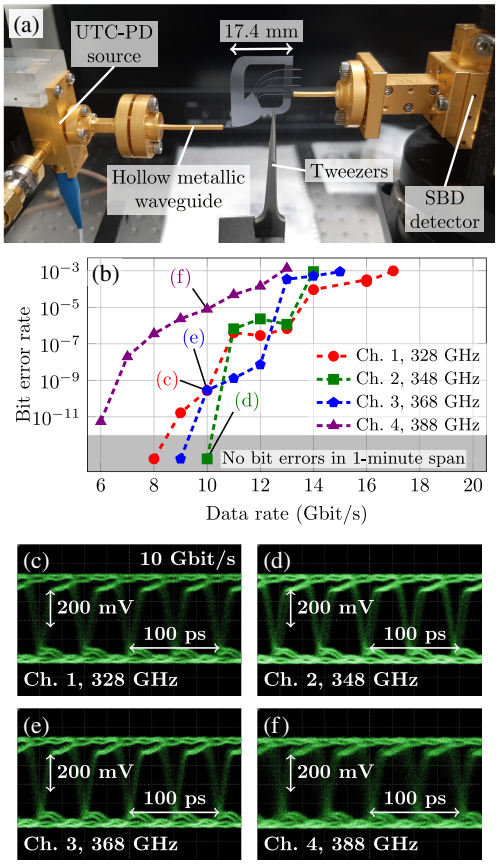

Fig. 5. Demonstration of terahertz communications, showing (a) a photograph of the experiment, in which Channel 4 is employed, (b) measured bit-error rates for all channels, and (c)–(f) eye diagrams of demodulated signal at 10 Gbit/s, for each channel.

extracts the terahertz-range beat frequency of the laser signal via a nonlinear process of optical rectification [40]. The modulation is commuted to the rectified signal, therebyproducing a modulated terahertz signal for which the carrier corresponds to the beat frequency of the lasers. The resultant terahertz waves are subsequently conveyed to a hollow metallic waveguide output, and applied to the combined port of the tunneling multiplexer that is the main subject of this work. Following its transit through the terahertz multiplexer, the modulated terahertz signal is probed at one of the channel ports, which is coupled to a hollow metallic waveguide that serves as input to a zero-biased Schottky barrier diode (SBD)-based terahertz detector. This extracts the modulating signal via envelope detection. Thereafter, the demodulated pulses are amplified, clipped, and conveyed to an oscilloscope to display the eye diagram. A bit-error-rate tester is employed to quantitatively measure the quality of the channel in real-time. A photograph of this experiment is shown in Fig. 5(a).

For each channel, the center frequency is chosen as a carrier, the data rate is swept in increments of 1 Gbit/s, and the resultant bit error rate is measured. The results of this procedure are shown in Fig. 5(b), and it can be seen that data rates of several Gbit/s are supported by all channels. In previous work [15,17], data rates of 20–30 Gbit/s bit-error-free were supported by the same equipment, and, hence, it is certain that the limiting factor upon the data rate is the bandwidth of the multiplexer itself. It is noted that the bit error rate is greater for Channel 4, as the output power of the UTC-PD is decreased at higher frequencies [40], leading

to diminished SNR. Eye diagrams of the demodulated signal at 10 Gbit/s are extracted for each channel, and the results are shown in Figs. 5(c)–5(f). There is some minor ripple and distortion of the pulse shape, which is likely due to echo signals produced by reflections at interfaces. This causes some dispersion, but it can be seen that the "eye" remains clearly open in each case. A more thorough discussion of dispersion performance is given in Section S6 of Supplement 1 that accompanies this article.

A wired demonstration is preferred over a more-realistic wireless communications link in order to observe the performance and achievable bandwidth of the tunneling multiplexer device in isolation. In the future, advanced antenna structures [41,42] may be integrated directly with the tunneling multiplexer device to provide an interface to free-space. It is understood that achievable data rates will be affected in such a wireless communications link, owing to the atmospheric absorption of terahertz waves [7].

4. DISCUSSION AND CONCLUSION

We have introduced the concept of gratingless tunneling multiplexers and employed it to realize a diplexer, triplexer, and 4×1 multiplexer for terahertz waves—all of which are both highly compact and efficient owing to the in-slab beamforming technique that we introduced. The simplicity of this technique offers versatility beyond that which is shown in the present work. A designer may essentially specify a desired in-slab magnitude distribution that is mediated by a single physical parameter: waveguide-to-slab separation. Furthermore, the curvature of the waveguide may be optimized, e.g., using Gerchberg–Saxton hologram-like techniques [43] to project near-arbitrary beam shapes into the slab.

The employed contactless power-transfer mechanism innately minimizes disturbance to fields within the tunneling waveguide, in a manner analogous to the advantage that uniform leaky-wave antennas have over those that are loaded with periodic radiators; the latter is always impacted by in-guide reflection from the radiating elements [44]. Our gratingless tunneling multiplexer devices hold the same advantage over sidewall-grating-based compact photonic multiplexers [23–25]. In addition to being contactless, the demonstrated devices are also substrateless, which means that the tunneling waveguide is essentially free-floating. For this reason, innovative effective-medium techniques and frame structures are sought in order to provide physical support without negatively impacting electromagnetic functionality.

The developed four-channel multiplexer is deployed in a demonstration of terahertz communications in order to clearly illustrate its applicability to its intended application and determine the limitation that the multiplexer's bandwidth and dispersion will impose. If we consider a bit error rate of 10^{-3} to be the limit of acceptable channel performance, then the achieved total capacity of the multiplexer is 48 Gbit/s using on–off keying, and this may be increased further with multi-level modulation techniques. That said, each channel was probed individually in experiment due to practical constraints including physical clearances, and for this reason, the experiment did not account for crosstalk. For this reason, a theoretical, quantitative investigation into the impact of crosstalk is undertaken, as detailed in Section S7 of Supplement 1. The results of this procedure show a signal-to-interference ratio of 10–20 dB for the 4×1 multiplexer, which is likely to adversely impact the quality of communications links. For this reason, it is critical to improve the isolation of the tunneling multiplexer, and this may be achieved by the incorporation of integrated terahertz-range filters or by refinements to the channel spacing and the interface between the slab and the channel ports. It is also noted that the analysis of crosstalk that is detailed in Supplement 1 assumes that the detector exhibits infinite bandwidth, as a coarse approximation of the broadband SBD that serves as a detector in the communications experiment that is detailed in Section 3.C. On the other hand, if coherent down-conversion were employed, then the interfering signals from other channels could be straightforwardly rejected by means of filtering at the baseband/IF stage, thereby enhancing the signal-to-interference ratio. Finally, the impact of the interference may be diminished with nonlinear devices including a limiting amplifier, as well as digital signals processing techniques.

Direct channelization at terahertz wavelengths facilitates power combining of several independent terahertz sources that operate at distinct carrier frequencies. This will increase the overall transmit power of a multi-channel terahertz link, which will be advantageous to terahertz communications given the well-known limitations upon transmit power [7]. We may alternatively discuss this in terms of the Shannon–Hartley theorem [45]; the data rate of a single channel is lowered, thereby reducing the SNR that is required to reliably convey information and increasing achievable transmit range. Overall data rate is compensated by aggregation of multiple reduced-bandwidth channels. This is the reason why terahertz-range link budget calculations often assume a dense frequency-division channelization scheme and specify a nominal transmit power per channel [46]. Furthermore, the thermal noise power of a given receiver is inversely proportional to overall bandwidth. A dense channelization scheme will therefore increase SNR by reducing this thermal noise.

Aside from power combining and noise reduction, there are other practical benefits to direct terahertz-frequency channelization. It is noteworthy that contemporary state-of-the-art all-electronic high-frequency communications systems have been reported that exhibit radio-frequency (RF) bandwidths of ~30 GHz [47]. On the other hand, the absolute spectral bandwidth that is covered by the terahertz tunneling multiplexer device is ~90 GHz, and this will increase proportionally if deployed at higher terahertz frequencies, i.e., by physical scaling. If this entire bandwidth were to be processed with a single baseband or IF system, then that system would necessarily utilize highly specialized mm-wave technologies. Furthermore, advanced terahertz mixers [48] that exhibit broad RF bandwidth would be required for frequency conversion. On the other hand, passive multiplexers divide the large RF bandwidth into manageable contiguous blocks, and, as a result, commercial off-the-shelf microwave-range components may be utilized in order to process the baseband/IF signal of each individual channel. The use of several commonplace electronic microwave-range systems in parallel (i.e., one for each channel) will be significantly more cost effective and practical than a single advanced broadband mm-wave system. An alternative, optoelectronic approach can similarly eschew electronic processing of the entire RF bandwidth by performing channelization in the optical domain, i.e., with beating laser signals that are individually modulated with microwave-range channel bandwidth and are subsequently down-converted to terahertz waves by means of photomixers [5,6]. However, there is a tradeoff in complexity, as this approach necessitates laser equipment. Furthermore, photomixing sources are typically of lower power than all-electronic approaches, and this channelization technique is not amenable to power combining of the sort that is described above. For these reasons, we

contend that passive terahertz-range frequency-division channelization schemes will be vital for the future of wireless terahertz communications. Furthermore, increasing the number of channels will enhance these benefits. In addition to high-volume communications, terahertz tunneling multiplexers may also find applications in multi-color imaging [49], and in terahertz tag technology [50].

It is stated in Section 3.B that the number of channels may be increased by lengthening the tunneling waveguide portion of the device. Another avenue to increase the number of channels is to extend the total frequency span of the scanning focus, and, to this end, it is necessary to understand present limitations upon bandwidth. The information in Figs. 1(e) and 1(g) shows that the tunneling waveguide becomes less dispersive at high frequencies, and so frequency scanning slows to the point where different frequencies cannot be distinguished with a tapered waveguide flare. On the other hand, it can be seen in Fig. 1(f) that the rate of leakage increases progressively as frequency is decreased. Thus, for low frequencies, the power is leaked too rapidly to allow for a broad aperture to develop, and so a high-quality focus is not formed. Total bandwidth may therefore be increased with careful optimization of parameters such as waveguide width w, starting separation s (0), silicon thickness t, and center-frequency selection in order to mediate between these two constraining phenomena. It may also be possible to modify the waveguide-slab interface, i.e., with effective-medium techniques, in order to engineer a rate of leakage that is near constant with respect to frequency to address the aforementioned lower-frequency limit.

Finally, we observe that, as the demonstrated tunneling multiplexer device is entirely passive, it may be adapted for operation in other frequency ranges. For instance, infrared-range operation will be achieved in a similarly all-dielectric device if implemented in a nano-scale photonic integrated circuit platform using generic foundry processes [51]. The benefits of our gratingless approach could therefore be realized at telecom wavelengths, in order to increase integration density, bandwidth, and efficiency. At lower frequencies, an equivalent mm-wave device could potentially be implemented in an RF circuitboard, in which microstrip lines replace the dielectric waveguides, and the free-propagation region is implemented with a parallel-plate waveguide, in a manner analogous to a Rotman lens [52]. As such, the tunneling multiplexer concept is of general utility across the electromagnetic spectrum.

Funding. Core Research for Evolutional Science and Technology (JPMJCR1534); Ministry of Education, Culture, Sports, Science and Technology (20H01064); Australian Research Council (DP180103561).

Acknowledgment. The Quadro P6000 GPU used for this research was contributed by NVIDIA Corporation to the Terahertz Engineering Laboratory, The University of Adelaide.

Disclosures. The authors declare no conflicts of interest.

Data Availability. Data underlying the results presented in this paper are not publicly available at this time but may be obtained from the authors upon reasonable request.

Supplemental document. See Supplement 1 for supporting content.

REFERENCES

1. H.-J. Song and T. Nagatsuma, "Present and future of terahertz communications," IEEE Trans. Terahertz Sci. Technol. **1**, 256–263 (2011).
2. T. Nagatsuma, G. Ducournau, and C. C. Renaud, "Advances in terahertz communications accelerated by photonics," Nat. Photonics **10**, 371–379 (2016).
3. T. S. Rappaport, Y. Xing, O. Kanhere, S. Ju, A. Madanayake, S. Mandal, A. Alkhateeb, and G. C. Trichopoulos, "Wireless communications and applications above 100 GHz: opportunities and challenges for 6G and beyond," IEEE Access **7**, 78729–78757 (2019).
4. P. Yang, Y. Xiao, M. Xiao, and S. Li, "6G wireless communications: vision and potential techniques," IEEE Network **33**, 70–75 (2019).
5. X. Yu, R. Asif, M. Piels, D. Zibar, M. Galili, T. Morioka, P. U. Jepsen, and L. K. Oxenløwe, "400-GHz wireless transmission of 60-Gb/s Nyquist-QPSK signals using UTC-PD and heterodyne mixer," IEEE Trans. Terahertz Sci. Technol. **6**, 765–770 (2016).
6. K. Takiguchi, "40 Gsymbol/s channel-based Nyquist wavelength division multiplexing communication in a terahertz-band using optical-domain reception signal processing," OSA Continuum **3**, 2308–2319 (2020).
7. C. M. Armstrong, "The truth about terahertz," IEEE Spectrum **49**, 36–41 (2012).
8. N. J. Karl, R. W. McKinney, Y. Monnai, R. Mendis, and D. M. Mittleman, "Frequency-division multiplexing in the terahertz range using a leaky-wave antenna," Nat. Photonics **9**, 717–720 (2015).
9. J. Ma, N. J. Karl, S. Bretin, G. Ducournau, and D. M. Mittleman, "Frequency-division multiplexer and demultiplexer for terahertz wireless links," Nat. Commun. **8**, 729 (2017).
10. A. Gonzalez, T. Kojima, K. Kaneko, and S. Asayama, "275–500 GHz waveguide diplexer to combine local oscillators for different frequency bands," IEEE Trans. Terahertz Sci. Technol. **7**, 669–676 (2017).
11. X. Zhao, O. Glubokov, J. Campion, A. Gomez-Torrent, A. Krivovitca, U. Shah, and J. Oberhammer, "Silicon micromachined D-band diplexer using releasable filling structure technique," IEEE Trans. Microw. Theory Technol. **68**, 3448–3460 (2020).
12. C. M. Yee and M. S. Sherwin, "High-Q terahertz microcavities in silicon photonic crystal slabs," Appl. Phys. Lett. **94**, 154104 (2009).
13. K. Tsuruda, M. Fujita, and T. Nagatsuma, "Extremely low-loss terahertz waveguide based on silicon photonic-crystal slab," Opt. Express **23**, 31977–31990 (2015).
14. W. Gao, X. Yu, M. Fujita, T. Nagatsuma, C. Fumeaux, and W. Withayachumnankul, "Effective-medium-cladded dielectric waveguides for terahertz waves," Opt. Express **27**, 38721–38734 (2019).
15. D. Headland, M. Fujita, and T. Nagatsuma, "Bragg-mirror suppression for enhanced bandwidth in terahertz photonic crystal waveguides," IEEE J. Sel. Top. Quantum Electron. **26**, 4900109 (2020).
16. Y. Yang, Y. Yamagami, X. Yu, P. Pitchappa, J. Webber, B. Zhang, M. Fujita, T. Nagatsuma, and R. Singh, "Terahertz topological photonics for on-chip communication," Nat. Photonics **14**, 446–451 (2020).
17. D. Headland, W. Withayachumnankul, X. Yu, M. Fujita, and T. Nagatsuma, "Unclad microphotonics for terahertz waveguides and systems," J. Lightwave Technol. **38**, 6853–6862 (2020).
18. W. Gao, W. S. L. Lee, X. Yu, M. Fujita, T. Nagatsuma, C. Fumeaux, and W. Withayachumnankul, "Characteristics of effective-medium-cladded dielectric waveguides," IEEE Trans. Terahertz Sci. Technol. **11**, 28–41 (2020).
19. H. Takahashi, Y. Hibino, and I. Nishi, "Polarization-insensitive arrayed-waveguide grating wavelength multiplexer on silicon," Opt. Lett. **17**, 499–501 (1992).
20. T. Fukazawa, F. Ohno, and T. Baba, "Very compact arrayed-waveguide-grating demultiplexer using Si photonic wire waveguides," Jpn. J. Appl. Phys. **43**, L673–L675 (2004).
21. J. Zou, X. Ma, X. Xia, J. Hu, C. Wang, M. Zhang, T. Lang, and J.-J. He, "High resolution and ultra-compact on-chip spectrometer using bidirectional edge-input arrayed waveguide grating," J. Lightwave Technol. **38**, 4447–4453 (2020).
22. T. Ohyama, Y. Doi, W. Kobayashi, S. Kanazawa, T. Tanaka, K. Takahata, A. Kanda, T. Kurosaki, T. Ohno, H. Sanjoh, and T. Hashimoto, "Compact hybrid-integrated 100-Gb/s TOSA using EADFB laser array and AWG multiplexer," IEEE Photon. Technol. Lett. **28**, 802–805 (2016).
23. P. Cheben, P. J. Bock, J. H. Schmid, J. Lapointe, S. Janz, D.-X. Xu, A. Densmore, A. Delâge, B. Lamontagne, and T. J. Hall, "Refractive index engineering with subwavelength gratings for efficient microphotonic couplers and planar waveguide multiplexers," Opt. Lett. **35**, 2526–2528 (2010).
24. J. Schmid, P. Cheben, P. Bock, R. Halir, J. Lapointe, S. Janz, A. Delage, A. Densmore, J.-M. Fedeli, T. Hall, R. Ma, I. Molina-Fernandez, and D.-X. Xu, "Refractive index engineering with subwavelength gratings in silicon microphotonic waveguides," IEEE Photon. J. **3**, 597–607 (2011).

25. P. J. Bock, P. Cheben, J. H. Schmid, A. V. Velasco, A. Delâge, S. Janz, D.-X. Xu, J. Lapointe, T. J. Hall, and M. L. Calvo, "Demonstration of a curved sidewall grating demultiplexer on silicon," Opt. Express **20**, 19882–19892 (2012).
26. F. Horst, W. M. Green, B. J. Offrein, and Y. A. Vlasov, "Silicon-on-insulator echelle grating WDM demultiplexers with two stigmatic points," IEEE Photon. Technol. Lett. **21**, 1743–1745 (2009).
27. C. Gilles, L. J. Orbe, G. Carpintero, G. Maisons, and M. Carras, "Mid-infrared wavelength multiplexer in InGaAs/InP waveguides using a Rowland circle grating," Opt. Express **23**, 20288–20296 (2015).
28. P. J. Whiteside, B. S. Goldschmidt, R. Curry, and J. A. Viator, "Controlled laser delivery into biological tissue via thin-film optical tunneling and refraction," Proc. SPIE **9303**, 93030O (2015).
29. J. Hu and C. R. Menyuk, "Understanding leaky modes: slab waveguide revisited," Adv. Opt. Photon. **1**, 58–106 (2009).
30. A. Hadij-El Houati, P. Cheben, A. Ortega-Monux, J. G. Wangüemert-Pérez, R. Halir, J. H. Schmid, and Í. Molina-Fernández, "Distributed Bragg deflector coupler for on-chip shaping of optical beams," Opt. Express **27**, 33180–33193 (2019).
31. D. Headland, M. Fujita, and T. Nagatsuma, "Half-Maxwell fisheye lens with photonic crystal waveguide for the integration of terahertz optics," Opt. Express **28**, 2366–2380 (2020).
32. D. Headland, Y. Monnai, D. Abbott, C. Fumeaux, and W. Withayachumnankul, "Tutorial: terahertz beamforming, from concepts to realizations," APL Photon. **3**, 051101 (2018).
33. H. Matsumoto, I. Watanabe, A. Kasamatsu, and Y. Monnai, "Integrated terahertz radar based on leaky-wave coherence tomography," Nat. Electron. **3**, 122–129 (2020).
34. V. Nourrit, J. L. Bougrenet de la Tocnaye, and P. Chanclou, "Propagation and diffraction of truncated Gaussian beams," J. Opt. Soc. Am. A **18**, 546–556 (2001).
35. R. W. McKinney, Y. Monnai, R. Mendis, and D. Mittleman, "Focused terahertz waves generated by a phase velocity gradient in a parallel-plate waveguide," Opt. Express **23**, 27947–27952 (2015).
36. I. Ohtera, "Diverging/focusing of electromagnetic waves by utilizing the curved leakywave structure: application to broad-beam antenna for radiating within specified wide-angle," IEEE Trans. Antennas Propag. **47**, 1470–1475 (1999).
37. A. V. Mazur and M. M. Gasik, "Thermal expansion of silicon at temperatures up to 1100°C," J. Mater. Process. Technol. **209**, 723–727 (2009).
38. D. W. Vogt, A. H. Jones, and R. Leonhardt, "Thermal tuning of silicon terahertz whispering-gallery mode resonators," Appl. Phys. Lett. **113**, 011101 (2018).
39. A. M. Wong and G. V. Eleftheriades, "An optical super-microscope for far-field, real-time imaging beyond the diffraction limit," Sci. Rep. **3**, 1715 (2013).
40. T. Nagatsuma, K. Oogimoto, Y. Yasuda, Y. Fujita, Y. Inubushi, S. Hisatake, A. M. Agoues, and G. C. Lopez, "300-GHz-band wireless transmission at 50 Gbit/s over 100 meters," in *Proc. IRMMW-THz* (IEEE, 2016).
41. W. Withayachumnankul, R. Yamada, M. Fujita, and T. Nagatsuma, "All-dielectric rod antenna array for terahertz communications," APL Photon. **3**, 051707 (2018).
42. D. Headland, W. Withayachumnankul, R. Yamada, M. Fujita, and T. Nagatsuma, "Terahertz multi-beam antenna using photonic crystal waveguide and Luneburg lens," APL Photon. **3**, 126105 (2018).
43. D. Wen, F. Yue, G. Li, G. Zheng, K. Chan, S. Chen, M. Chen, K. F. Li, P. W. H. Wong, K. W. Cheah, E. Y. B. Pun, S. Zhang, and X. Chen, "Helicity multiplexed broadband metasurface holograms," Nat. Commun. **6**, 8241 (2015).
44. M. Guglielmi and D. Jackson, "Broadside radiation from periodic leaky-wave antennas," IEEE Trans. Antennas Propag. **41**, 31–37 (1993).
45. C. E. Shannon, "A mathematical theory of communication," Bell Syst. Tech. J. **27**, 379–423 (1948).
46. T. Schneider, A. Wiatrek, S. Preußler, M. Grigat, and R.-P. Braun, "Link budget analysis for terahertz fixed wireless links," IEEE Trans. Terahertz Sci. Technol. **2**, 250–256 (2012).
47. P. Rodrguez-Vázquez, J. Grzyb, B. Heinemann, and U. R. Pfeiffer, "A 16-QAM 100-Gb/s 1-m wireless link with an EVM of 17% at 230 GHz in an SiGe technology," IEEE Microw. Wirel. Compon. Lett. **29**, 297–299 (2019).
48. Y. He, Y. Tian, L. Miao, J. Jiang, and X. Deng, "A broadband 630–720 GHz Schottky based sub-harmonic mixer using intrinsic resonances of hammer-head filter," China Commun. **16**, 76–84 (2019).
49. K. Statnikov, J. Grzyb, B. Heinemann, and U. R. Pfeiffer, "160-GHz to 1-THz multi-color active imaging with a lens-coupled SiGe HBT chip-set," IEEE Trans. Microw. Theory Tech. **63**, 520–532 (2015).
50. Y. Kujime, M. Fujita, and T. Nagatsuma, "Terahertz tag using photonic-crystal slabs," J. Lightwave Technol. **36**, 4386–4392 (2018).
51. M.-C. Lo, A. Zarzuelo, R. Guzmán, and G. Carpintero, "Monolithically integrated microwave frequency synthesizer on InP generic foundry platform," J. Lightwave Technol. **36**, 4626–4632 (2018).
52. W. Rotman and R. Turner, "Wide-angle microwave lens for line source applications," IEEE Trans. Antennas Propag. **11**, 623–632 (1963).